ADVANCED MATERIALS
www.advmat.de

Unlocking the Ligand-Dominated Redox Activity in π–d Conjugated Coordination Polymers for High-Capacity and Stable Potassium Storage

Kang Han, Zhenhang Zhong, Hao Zhang, Guangwan Zhang, Xuanpeng Wang, Fang Liu, Chaojiang Niu, and Liqiang Mai**

Potassium-ion batteries (KIBs) offer a cost-effective, resource-abundant alternative to lithium-ion systems, yet the development of high-performance anodes with adequate capacity, stability, and rate capability remains a major challenge. Here, an electronic structure engineering strategy is introduced via d-orbital configuration optimization in a novel class of π–d conjugated coordination polymers (TM-BTA, TM = Ni, Co, Mn). Orbital-level and charge density analyses reveal that the metal center's electronic configuration governs metal–ligand interaction strength, thereby modulating charge delocalization and ligand redox behavior. Among the series, Ni^{2+} exhibits the strongest π–d conjugation with nitrogen donor atoms, stabilizing C=N bonds and enabling highly reversible C=N/C—N transformations as the dominant redox process. This optimized coordination lowers the K^+ adsorption energy barrier by 44% compared to Co^{2+} and Mn^{2+}, markedly improving kinetics. As a result, Ni-BTA delivers a high reversible capacity of 452 mAh g^{-1} with 99.2% retention over 500 cycles at 100 mA g^{-1}, and maintains 292 mAh g^{-1} after 4,000 cycles at 1,000 mA g^{-1}. In situ spectroscopy and DFT calculations reveal a ligand-centered three-electron redox mechanism, where nitrogen heterocycles dominate K^+ storage and electrochemically inert Ni centers maintain structural integrity. This work establishes a general design principle for KIB anodes via d-orbital engineering in coordination polymers.

1. Introduction

The rapid evolution of portable electronics and grid-scale energy storage has intensified the demand for sustainable, high-performance battery systems beyond conventional lithium-ion technologies.[1–3] While lithium-ion batteries (LIBs) currently dominate the market, geopolitical constraints on lithium reserves (merely 0.006% of Earth's crust) and soaring extraction costs (300% increase since 2020) necessitate urgent exploration of alternative chemistries. Potassium-ion batteries (KIBs) have emerged as a compelling candidate, leveraging Earth-abundant potassium resources (2.09% crustal abundance) and comparable redox potential (−2.93 V vs. SHE) to lithium systems.[4–7] Crucially, KIBs exhibit enhanced ionic transport kinetics (K^+ Stokes radius: 3.6 Å in propylene carbonate vs. 4.8 Å for Li^+) and reduced dendrite formation propensity, making them particularly suitable for high-power applications.[8–11] However, the large ionic radius of K^+ (1.38 Å vs 0.76 Å for Li^+) induces severe structural deformation (>300% volume expansion) in conventional anodes, resulting in rapid capacity decay (<100 cycles for graphite) and limited energy density (<200 mAh g^{-1} for most intercalation materials).[8–11]

Among various research avenues for KIB development, the rational design of anode materials has become critical. Commercial KIB graphite anodes exhibit unsatisfactory potassium storage capability (specific capacity <280 mAh g^{-1}) due to

K. Han, Z. Zhong, H. Zhang, G. Zhang, F. Liu, L. Mai
State Key Laboratory of Advanced Technology for Materials Synthesis and Processing
School of Materials Science and Engineering
Wuhan University of Technology
Wuhan 430070, P.R. China
E-mail: mlq518@whut.edu.cn

X. Wang
Department of Physical Science & Technology
School of Physics and Mechanics
Wuhan University of Technology
Wuhan 430070, P. R. China

The ORCID identification number(s) for the author(s) of this article can be found under https://doi.org/10.1002/adma.202509022

DOI: 10.1002/adma.202509022

K. Han, X. Wang
Hubei Longzhong Laboratory
Wuhan University of Technology (Xiangyang Demonstration Zone)
Xiangyang, Hubei 441000, P. R. China

X. Wang
Zhongyu Feima New Material Technology Innovation Center (Zhengzhou) Co. Ltd.
High Technology Industrial Development Zone
No. 60 Xuelan Road, Zhengzhou, Henan 450001, P. R. China

K. Han, C. Niu
School of Materials Science and Engineering
Zhengzhou University
Zhengzhou 450001, P. R. China
E-mail: niuchaojiang@zzu.edu.cn

insufficient interlayer spacing for K^+ accommodation.[12–14] While small organic molecules were initially considered, their inherent limitations in structural stability and insufficient electron transport capacity under electrochemical cycling hindered practical applications.[15–17] This has driven intensive research into advanced organic polymer materials, with three predominant material paradigms emerging: Metal-organic frameworks (MOFs) offering tunable pore structures for K^+ accommodation,[18–21] covalent organic frameworks (COFs) with designer π-conjugated systems for redox activity,[6,22–25] and conjugated coordination polymers (CCPs) that uniquely integrate metallic conductivity with molecular-level redox tunability.[26–30]

Among these, CCPs represent a significant advancement through their distinctive π–d orbital hybridization, an electronic coupling phenomenon where transition metal (TM) d-orbitals interact with ligand π-antibonding orbitals, enabling exceptional charge delocalization. This unique mechanism successfully resolves the longstanding conductivity-stability trade-off plaguing organic electrodes, achieving remarkable electrical conductivity while maintaining structural integrity.[29,31,32] For instance, Takaishi et al. constructed a $Cu[Cu(pdt)_2]$ unit combining electron donor and acceptor components, forming a tetrahedral lattice with nitrogen atoms coordinating Cu^{2+}. This structure supports bond-conducted electron transfer, while weak van der Waals interactions facilitate rapid charge carrier migration within the 2D layered structure.[33] Additionally, the unpaired electrons in Cu^{2+} further enhance conductivity, achieving 6×10^{-4} S cm^{-1} at 300 K. Wang et al. used Cu^{2+} with bistable coordination configurations as metal nodes to construct a π–d conjugated chain structure, forming a 3D CCPs (Cu-TAPT) through tetrahedral connections, achieving single-crystal conductivity up to 400 S m^{-1}.[34] Consequently, compared to traditional organic materials, CCPs exhibit higher theoretical capacities and substantial performance potential. However, despite these prospects, several scientific challenges must be addressed to fully unlock the potential of CCPs in KIBs. The primary challenge lies in understanding their precise redox behavior, especially the roles of transition metals and ligands during K^+ insertion/extraction. Additional challenges include ensuring the stability of π–d conjugated frameworks during large-scale ion insertion/extraction, mitigating possible side reactions, and maintaining long-term cycling stability. To maximize the potential of π–d conjugated polymers in KIBs, systematic investigation of their electrochemical mechanisms and structural evolution during operation is essential.

To address these challenges, we propose an electronic-structure engineering strategy based on tuning d-orbital interactions in π–d conjugated polymers. By coordinating 1,2,4,5-benzenetetramine (BTA) with closed-shell d^8 Ni^{2+} under ammonia, we constructed a novel CCPs (Ni-BTA) exhibiting exceptional stability and redox activity. In contrast to Co^{2+} and Mn^{2+} analogues, where unpaired electrons and Jahn–Teller distortions weaken the framework, the filled d^8 shell of Ni^{2+} (i) strengthens π–d overlap with the ligand to stabilize antibonding levels, (ii) promotes σ–π coupling that lowers the K^+ adsorption barrier, and (iii) remains redox-inactive to preserve structural integrity. The optimized Ni-BTA achieves exceptional performance: 452 mAh g^{-1} capacity retention over 500 cycles (99.2%) at 100 mA g^{-1}, and 292 mAh g^{-1} after 4000 cycles at 1000 mA g^{-1} – surpassing most reported organic/polymeric anodes in cycle stability. Through multimodal in situ characterization and theoretical modeling, we elucidate a ligand-centered three-electron redox mechanism, establishing a new design principle for stable high-capacity KIB electrodes.

2. Results and Discussion

2.1. Structural Properties of TM-BTA

The TM-BTA conjugated coordination polymers were synthesized using planar 1,2,4,5-benzenetetramine (BTA·4HCl) as the central ligand and transition metal ions (TM^{2+} = Ni^{2+}, Co^{2+}, Mn^{2+}) as active centers under concentrated ammonia and oxygen conditions (**Figure 1a**).[27,35] The pH-regulated deprotonation of BTA·4HCl by ammonia facilitates multidentate coordination with TM^{2+}, inducing linear chain alignment through ligand-directing effects. Structural optimization through first-principles calculations reveals planar fused aromatic backbones where TM^{2+} ions coordinate two adjacent BTA molecules in planar four-coordinate configurations (Figure 1b). This geometric arrangement maintains molecular planarity and stabilizes electronic structures. Mayer bond order analysis demonstrates transition metal coordination activates C—N bonds in the BTA chain, with Ni-BTA exhibiting the strongest double-bond character (1.15 vs. 1.10 for Co-BTA and 1.07 for Mn-BTA), correlating with enhanced potassium storage capacity (Figure S1, Supporting information). Electronic structure analysis through total density of states (TDOS) and partial density of states (PDOS) reveals significant π–d conjugation in all TM-BTA polymers, characterized by substantial overlap between TM 3d and BTA 2p orbitals near the Fermi level (Figure 1c–e). For Ni-BTA, the pronounced hybridization between Ni 3d (d_{xz}/d_{yz}) orbitals and BTA π antibonding orbitals (Figure 1c and Figure S2, Supporting information) enables a unique $t_2g\rightarrow\pi$ back-donation mechanism. This electron delocalization stabilizes the BTA ligand's π^* system while strengthening Ni-N coordination bonds, as evidenced by the planar tetracoordinate geometry (Figure 1b) and Mayer bond order enhancement (1.15, Figure S1, Supporting information).[36] Bandgap analysis shows Ni-BTA possesses the narrowest highest occupied crystal orbital (HOCO)- lowest unoccupied crystal orbital (LUCO) gap (1.0 eV, Figure 1c), substantially smaller than Co-BTA (1.50 eV, Figure 1d) and Mn-BTA (2.01 eV, Figure 1e), indicating superior charge transport capability. The d-orbital PDOS further confirms stronger Ni 3d and BTA 2p orbital hybridization in Ni-BTA compared to its counterparts, with more concentrated density near the Fermi level (Figure 1f). Importantly, the closed-shell d^8 configuration of Ni^{2+} plays a pivotal role in enabling bidirectional charge regulation. The fully filled t_2g orbitals (d_{xz}, d_{yz}, d_{z^2}) allow symmetric π-backdonation to BTA ligands (Figure 1g and Figure S2, Supporting information), whereas the unoccupied $d_{x^2-y^2}$ orbital engages in σ-π hybridization with the ligand's π-system. This dual interaction synergistically reduces K^+ adsorption energy by delocalizing charge density across the conjugated framework. In contrast, d^7 configuration of Co^{2+} exhibits partial d_{xz} orbital occupancy, disrupting π-backdonation symmetry and weakening metal-ligand interactions (Figure 1g and Figure S3, Supporting information).[37] For Mn^{2+} (d^5 configuration), localized magnetic moments from unpaired electrons in π-symmetric orbitals induce ligand field distortions (Figure 1g

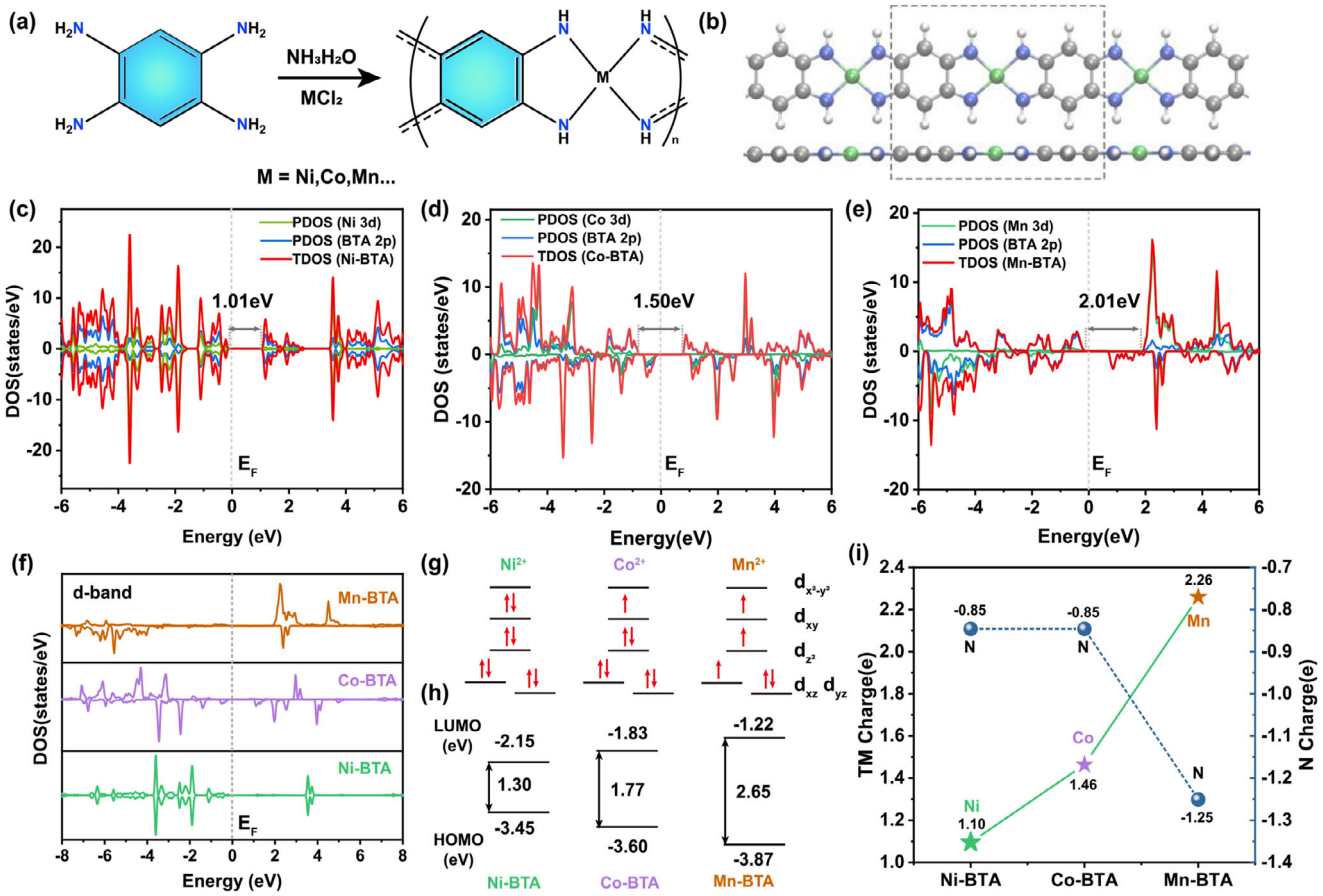

Figure 1. Identification of the structural properties of TM-BTA. a) General synthesis pathway for TM-BTA (TM = Ni, Co, Mn); b) Schematic representation of the planar conjugated coordination polymer of TM-BTA (side and top views); (c–e) TDOS and PDOS for TM-BTA: c) Ni-BTA, d) Co-BTA, e) Mn-BTA; f) PDOS for d-orbitals; g) Distribution characteristics of TM^{2+} valence electrons in TM-BTA; (h) HOMO-LUMO characteristics; i) Atomic charge characteristics.

and Figure S4, Supporting information), further degrading conjugation efficiency.

The progressive decline in electronic stability from Ni to Mn-BTA directly correlates with their charge transport properties. Ni-BTA exhibits the strongest d_{xz}/d_{yz} orbital hybridization with BTA 2p states near the Fermi level (Figure 1f), corresponding to its narrowest highest occupied molecular orbital (HOMO)-lowest unoccupied molecular orbital (LUMO) gap (1.30 vs. 1.77/2.65 eV for Co/Mn-BTA, Figure 1h). This optimized orbital alignment facilitates electron excitation and conductive pathway formation, as further evidenced by its favorable potassium adsorption energy (−0.54 vs. −0.97/−0.98 eV for Co/Mn-BTA, Figure S5, Supporting information). Charge distribution analysis (Figure 1i) quantitatively confirms these trends, with Ni centers showing the most effective charge transfer (residual charge 1.10 e) compared to Co (1.85 e) and Mn (2.26 e).

2.2. Structural Characterizations of TM-BTA

The morphological and structural features of TM-BTA coordination polymers were systematically investigated. Scanning electron microscopy (SEM) revealed that Ni-BTA exhibited a highly ordered nanoneedle morphology with nanowire diameters ranging from 0.5 to 1 μm (**Figures** 2a and S6, Supporting information). Co-BTA displayed a disordered bulk morphology, while Mn-BTA formed 2D nanosheet structures (Figure S6, Supporting information). Optical microscopy and powder X-ray diffraction (PXRD) analyses demonstrated that Ni-BTA and Mn-BTA surfaces developed crystalline domains after 10 min of gas-phase reaction, whereas Co-BTA showed weaker crystallinity (Figures S7 and S8, Supporting information). TEM images show that the diameter of the Ni-BTA nanowires is ≈15 nm (Figure S9a, Supporting information), and HR-TEM displays lattice fringes with a spacing of 2.03 Å, corresponding to the (042) plane identified in PXRD results (Figure 2b and Figure S9b, Supporting information). Density functional theory (DFT) simulations indicate that the experimentally prepared Ni-BTA aligns with the herringbone molecular packing structure (Figure 2c and Figure S10–S12, Supporting information).

The characteristic peaks at $2\theta = 14.5°$, 20.5°, 24.2°, 28.6°, 39.4°, and 43.8° can be indexed to the (011), (021), (030), (022), (042), and (033) planes, with interplanar distances of 5.8, 4.3, 3.7, 3.1, 2.3, and 2.1 Å, respectively (Figure 2d). This alignment may be attributed to relatively weak interactions between the BTA ligands and the Ni center, allowing the electronic structure of the

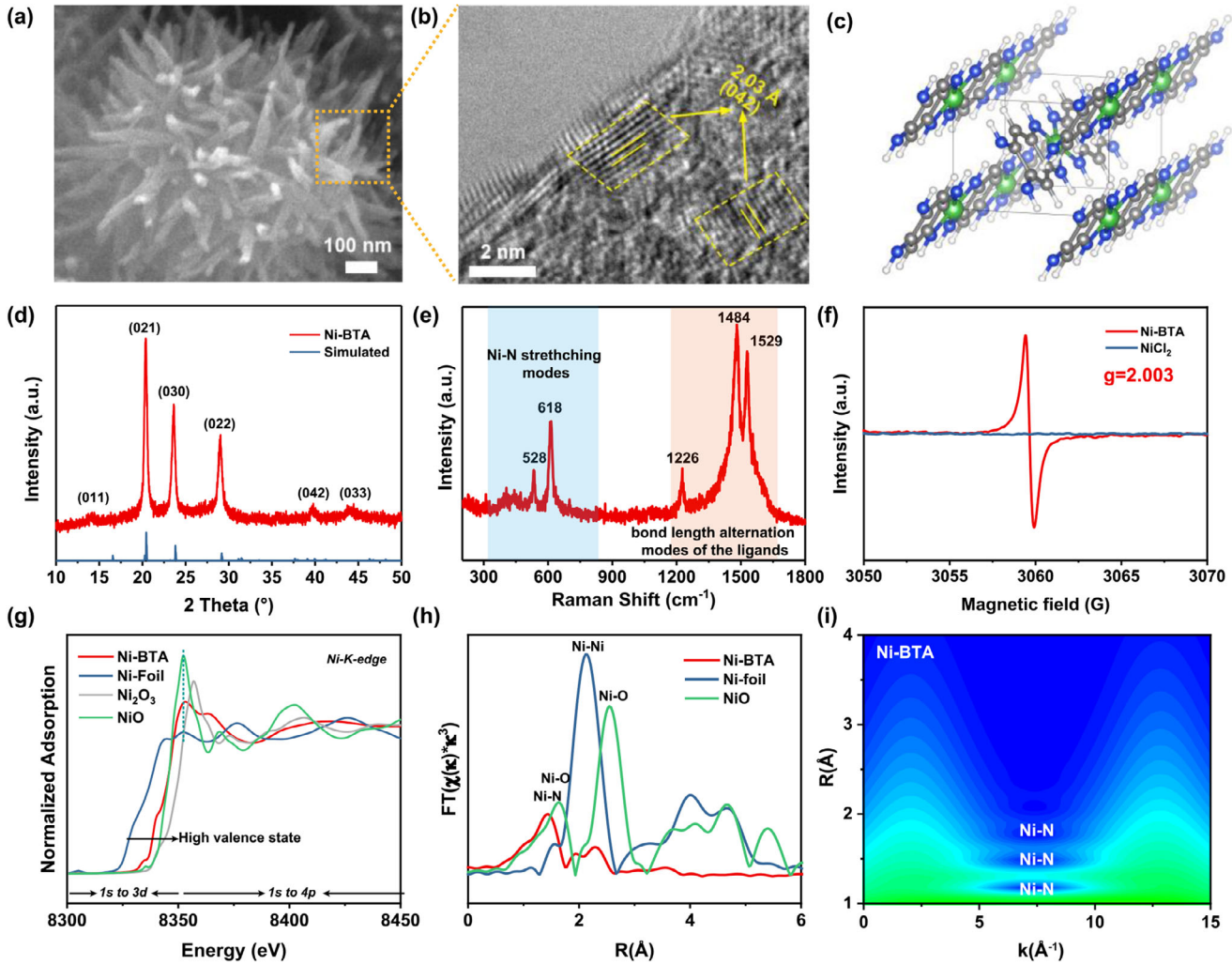

Figure 2. Structural characterizations of the Ni-BTA. a) Scanning electron microscopy (SEM) image of Ni-BTA; b) High-resolution transmission electron microscopy (HR-TEM) image and lattice fringe features; c) Molecular crystal packing; d) Comparison of experimental XRD with simulated results; e) Characteristic Raman vibrational spectrum; f) EPR distribution; g–i) Synchrotron radiation characteristic spectra of Ni-BTA: (g) K-edge XANES spectrum of Ni; (h) Fourier transform (FT) of the EXAFS spectrum of Ni, k^3-weighted $\chi(k)$ function; (i) Wavelet transform spectrum of Ni.

ligands to dominate the stacking behavior, resulting in a herringbone arrangement that minimizes total energy.[38] To probe the molecular interactions within Ni-BTA, electron localization function (ELF) and interaction region indicator (IRI) analyses were conducted,[39,40] identifying weak coupling interactions between the Ni center and BTA ligand, as well as the π–π stacking interactions typical of herringbone packing (Figure S13 and S14, Supporting information). These analyses indicate that the molecular stabilization of Ni-BTA is achieved through a combination of hydrogen bonding, π–d conjugation, and weak van der Waals forces. Further orbital interaction analysis shows an extensive distribution of π orbital density near the HOMO within the Ni-BTA chain, emphasizing the structural role of π bonds and the highly delocalized nature of π electrons (Figure S15, Supporting information). Additionally, frontier molecular orbital analysis reveals that the HOMO and LUMO are primarily localized on the BTA ligand rather than on the Ni center. This suggests that the ligand predominantly determines the electronic properties and chemical reactivity of the molecule, while the Ni atom primarily serves as a structural support, stabilizing the molecular configuration rather than directly participating in electron transfer or chemical reactions. This finding aligns with the ELF analysis, highlighting the weak coupling between Ni^{2+} and the ligand.

Thermogravimetric analysis (TGA) and CHNO elemental analysis further confirm the high crystallinity and stability of the Ni-BTA crystal. The TGA curve shows that Ni-BTA maintains thermal stability up to 360°C, underscoring the robustness of the Ni-N_4 coordination framework. Correspondingly, Mn-BTA demonstrates thermal stability comparable to Ni-BTA, while Co-BTA exhibits the weakest thermal stability, further validating the influence of crystallinity on thermal resilience (Figure S16, Supporting information). Moreover, CHNO analysis verifies that the experimental composition closely matches the theoretical values for Ni, C, N, and H (Figure S17, Supporting information), further reflecting the ordered arrangement of the coordination structure. The C═N and C—N peaks observed in infrared (IR) spectra

confirm the activation of the C—N bond in BTA by Ni coordination (Figure S18, Supporting information). In the Raman spectra, vibration peaks at 258 and 618 cm^{-1} correspond to the stretching vibrations of the Ni-N bonds, while peaks in the 1200–1600 cm^{-1} region reflect the molecular vibrational modes of the BTA ligand (Figure 2e). Notably, the IR and Raman spectra of Co-BTA and Mn-BTA also exhibit similar structural features, further suggesting the universality of the conjugative interaction between coordination ions and the ligand (Figure S19, Supporting information). Electron paramagnetic resonance (EPR) spectroscopy was also employed to probe the electronic structure of Ni-BTA (Figure 2f). A distinct signal was observed at a g-value of 2.003, a value highly characteristic of an organic π-radical, suggesting the unpaired electron resides on the BTA ligand.[41,42] In contrast, $NiCl_2$, where the d-orbitals of Ni^{2+} are fully occupied, shows no EPR signal. In addition, synchrotron radiation X-ray absorption fine structure (XAFS) spectroscopy was employed to study the valence state and coordination structure of Ni-BTA. X-ray absorption near edge structure (XANES) spectra show that the absorption edge of Ni-BTA closely resembles that of divalent Ni in NiO, indicating that Ni predominantly exists in the Ni^{2+} in the Ni-BTA coordination structure (Figure 2g). Extended X-ray absorption fine structure (EXAFS) analysis further reveals significant differences between the coordination environment of Ni-BTA and those of NiO and Ni foil. Fourier transform results show that the Ni-N bond length is ≈1.76 Å, which is very close to the bond length obtained from both pair distribution function (1.81 Å) testing and theoretical calculations (1.83 Å) (Figure S20, Supporting information). This suggests that the Ni-N coordination structure is relatively dispersed. (Figure 2h). Wavelet transform analysis further demonstrates that the Ni-N coordination environment in Ni-BTA differs markedly from the strong Ni-Ni and Ni-O interactions observed in NiO and Ni foil, reflecting the weaker coordination interactions present in Ni-BTA (Figure 2i and Figure S21, Supporting information).

X-ray photoelectron spectroscopy (XPS) was further used to study the surface elemental composition, chemical state, and electronic structure of Ni-BTA. In the wide-scan XPS spectrum, significant peaks corresponding to Ni 2p, O 1, N 1, and C 1s were observed, and no Cl signal was detected, indicating the absence of Cl^- counterions in Ni-BTA (Figure S22a, Supporting information). In the high-resolution Ni 2p spectrum, peaks corresponding to Ni $2p_3/_2$ and Ni $2p_1/_2$ were observed at ≈855 and 873 eV, respectively, confirming that Ni exists predominantly in the divalent Ni^{2+} state in Ni-BTA (Figure S22b, Supporting information).[43–45] This finding is further validated by the peak observed at 860 eV in the electron energy loss spectrum (Figure S23, Supporting information).[46,47]

The C 1s spectrum features three peaks: C—C/C═C at 284.8 eV, C═N—Ni at ≈286.6 eV, and adventitious C═O at 288.6 eV (Figure S22c, Supporting information). The distinct C═N—Ni peak confirms the activation of C—N bonds, imparting them with double-bond character upon coordination. The N 1s spectrum is deconvoluted into uncoordinated amine-N (C—NH—C) at ≈399.2 eV and Ni-coordinated pyridinic-N at ≈397.5 eV (Figure S22d, Supporting information). The pronounced negative shift of the pyridinic-N peak serves as a direct spectroscopic signature of strong d-π^* back-donation, a key feature of the π–d conjugation in this system.[53,54] A smaller peak at ≈400.5 eV is attributed to satellite features. Collectively, these spectral assignments not only confirm the proposed structure but also highlight the electronic activation of the ligand framework through π–d conjugation.

2.3. Electrochemical Performance Evaluation

To explore the potential applications of the developed π–d conjugated polymers in KIBs, comprehensive assessments of the K storage performance of Ni-BTA, Co-BTA, and Mn-BTA samples were conducted. The initial cyclic voltammetry (CV) curves of the three samples revealed significant redox peaks only in Ni-BTA, likely due to enhanced crystallinity induced by its high coordination characteristics (**Figure 3**a).[27] Furthermore, Ni-BTA exhibited higher electrochemical activity, a property also reflected in the corresponding charge-discharge curves (Figure 3b). The CV curves of Ni-BTA (Figure S24, Supporting information) reveal an initial activation process. During the first cathodic scan, reduction peaks at 1.14 and 0.75 V are observed, which shift to ≈1.30 and 0.87 V in the subsequent cycle. This potential shift is attributed to electrochemical activation, encompassing SEI film formation and lattice relaxation. Subsequently, the CV curves from the third cycle onward show excellent overlap, signifying remarkable structural stability and highly reversible potassiation/depotassiation. Capacity performance analysis further revealed that the charge capacities of Ni-BTA were 712 and 398 mAh g^{-1}, respectively, with an initial Coulombic efficiency as high as 56%. The irreversible capacity observed during the first cycle is attributed to a combination of phenomena, primarily the formation of a solid electrolyte interphase (SEI), along with some electrolyte decomposition and reactions involving surface functionalities on the polymer.[48] During the initial 50 cycles, Ni-BTA demonstrated a notable capacity increase, consistent with the lattice activation process observed in the CV analysis. Remarkably, even after 500 cycles, Ni-BTA retained a high reversible capacity of 452 mAh g^{-1}, with a Coulombic efficiency approaching 100%. Relative to the maximum specific capacity of 500 mAh g^{-1} during cycling, Ni-BTA achieved a capacity retention rate of 99.2%, with a capacity decay rate of only 0.0016% per cycle (Figure 3c). This performance significantly exceeds that of Co-BTA and Mn-BTA in K storage activity (Figure 3c and Figures S25 and S26, Supporting information).

Rate performance tests further demonstrated the superior potassium storage capability of Ni-BTA across various charge-discharge currents (Figure 3d). At current densities of 50, 100, 200, 500, and 1000 mA g^{-1}, Ni-BTA exhibited high reversible specific capacities of 480, 422, 370, 312, and 253 mAh g^{-1}, respectively. When the current density was restored to 100 mA g^{-1}, the reversible specific capacity remained at 455 mAh g^{-1}. The corresponding rate capability charge-discharge curves confirmed that Ni-BTA consistently maintained efficient redox platform behavior across different current densities. Importantly, even at ultra-high current densities of 1000 mA g^{-1}, Ni-BTA retained a reversible specific capacity of 292 mAh g^{-1} after 4000 cycles, with a capacity retention rate of 90% and a capacity decay rate of only 0.0025% per cycle (Figure 3g). This performance is significantly better than that of Co-BTA (which exhibited a reversible specific capacity of only 120 mAh g^{-1} after 4000 cycles,

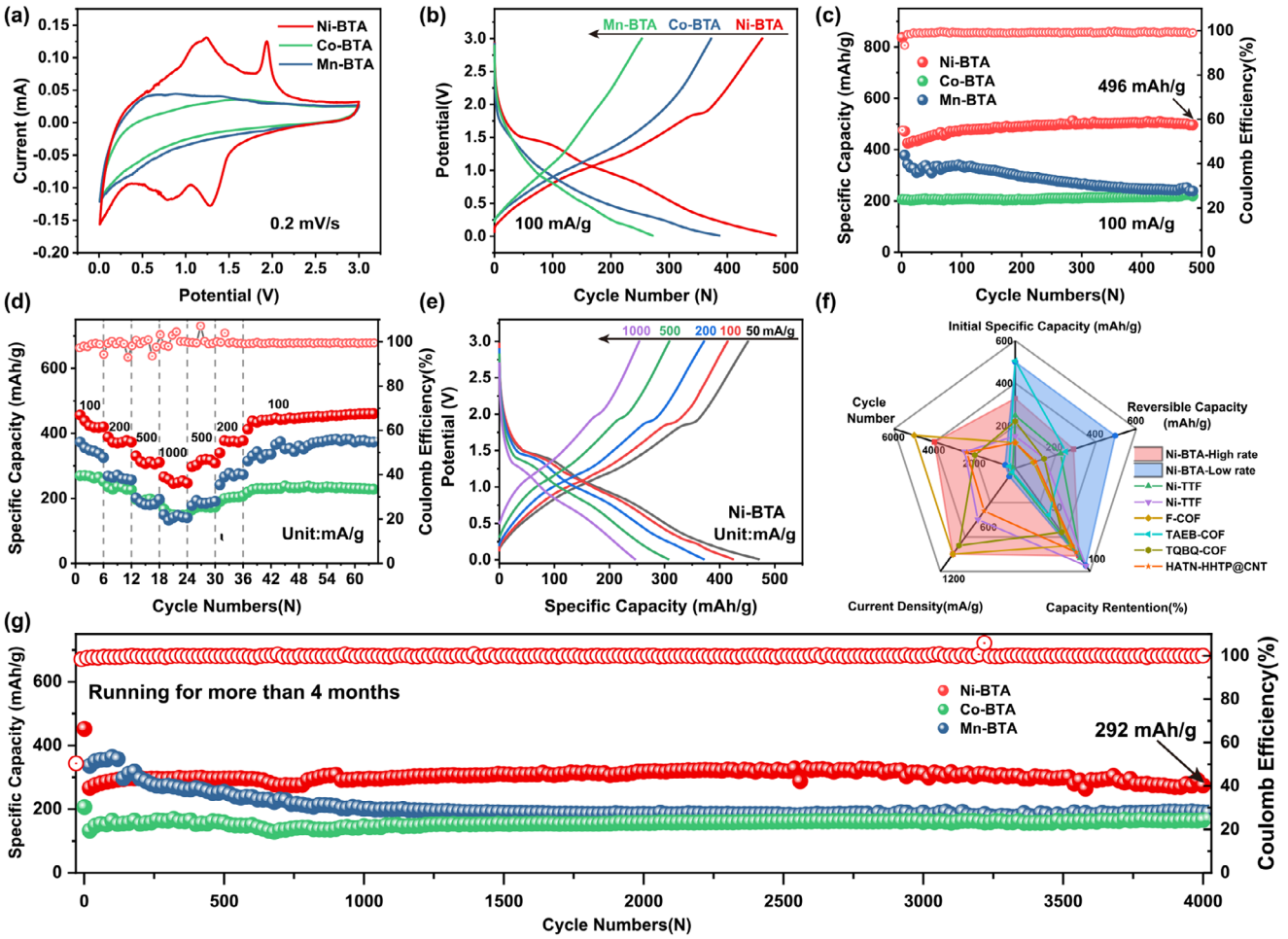

Figure 3. Electrochemical potassium storage characteristics of TM-BTA. a) CV curves; b) Characteristic charge-discharge curve; c) Reversible specific capacity and Coulombic efficiency at 100 mA g^{-1}; d) Rate performance characteristics; e) Characteristic charge-discharge curves of Ni-BTA at different current densities; f) 5D comparison of Ni-BTA performance with other reported polymer anodes; [6,24,49,50] g) Long cycling performance at 1000 mA g^{-1}.

with a capacity retention rate of 52%) and Mn-BTA (which exhibited a reversible specific capacity of only 186 mAh g^{-1} after 4000 cycles, with a capacity retention rate of 88%). Given these characteristics, a comparative analysis of Ni-BTA with other reported MOFs/COFs/CCPs for KIBs was conducted.[6,24,49,50] This comparison considered five key indicators: initial discharge specific capacity, cycle number, capacity retention rate, reversible specific capacity, and corresponding current density—indicating that Ni-BTA outperforms currently reported organic anode materials in both low and high current applications, further validating its outstanding structural stability and potassium storage performance (Figure 3f). To further contextualize this high performance, a Ragone plot is presented (Figure S28, Supporting information), where a theoretical full cell utilizing the Ni-BTA anode with a layered oxide cathode is projected to deliver a competitive energy density of ≈212 Wh kg^{-1},[55] highlighting its promising position among various energy storage technologies.

To further elucidate the kinetic origins of Ni-BTA's superior rate capability and overall electrochemical performance, Galvanostatic Intermittent Titration Technique (GITT) measurements were conducted to directly compare the K^+ diffusion kinetics across the TM-BTA series (Figure S29a–c, Supporting information). Across the majority of the charge and discharge potential range, the Ni-BTA electrode exhibits a consistently higher K^+ diffusion coefficient (D_{K^+}) compared to its Co-BTA and Mn-BTA counterparts (Figure S29d,f, Supporting information). The average log(D_{K^+}) values for Ni-BTA during discharge (−11.21) and charge (−11.06) are significantly higher than those for Co-BTA (−11.30 and −11.13) and Mn-BTA (−11.32 and −11.14), respectively (Figure S29e,g, Supporting information). This directly measured enhancement in ionic mobility provides a concrete explanation for the superior rate capability observed for Ni-BTA. The sluggish diffusion kinetics in Co-BTA and Mn-BTA, as quantified by their lower D_{K^+} values, can be attributed to the "thermodynamic traps" created by their excessively strong K^+ adsorption energies, which hinder ion transport. This synergy between moderated adsorption energy and enhanced diffusion kinetics is the key to Ni-BTA's exceptional balance of high capacity, excellent rate performance, and outstanding cycling stability, distinguishing it from the other analogues.

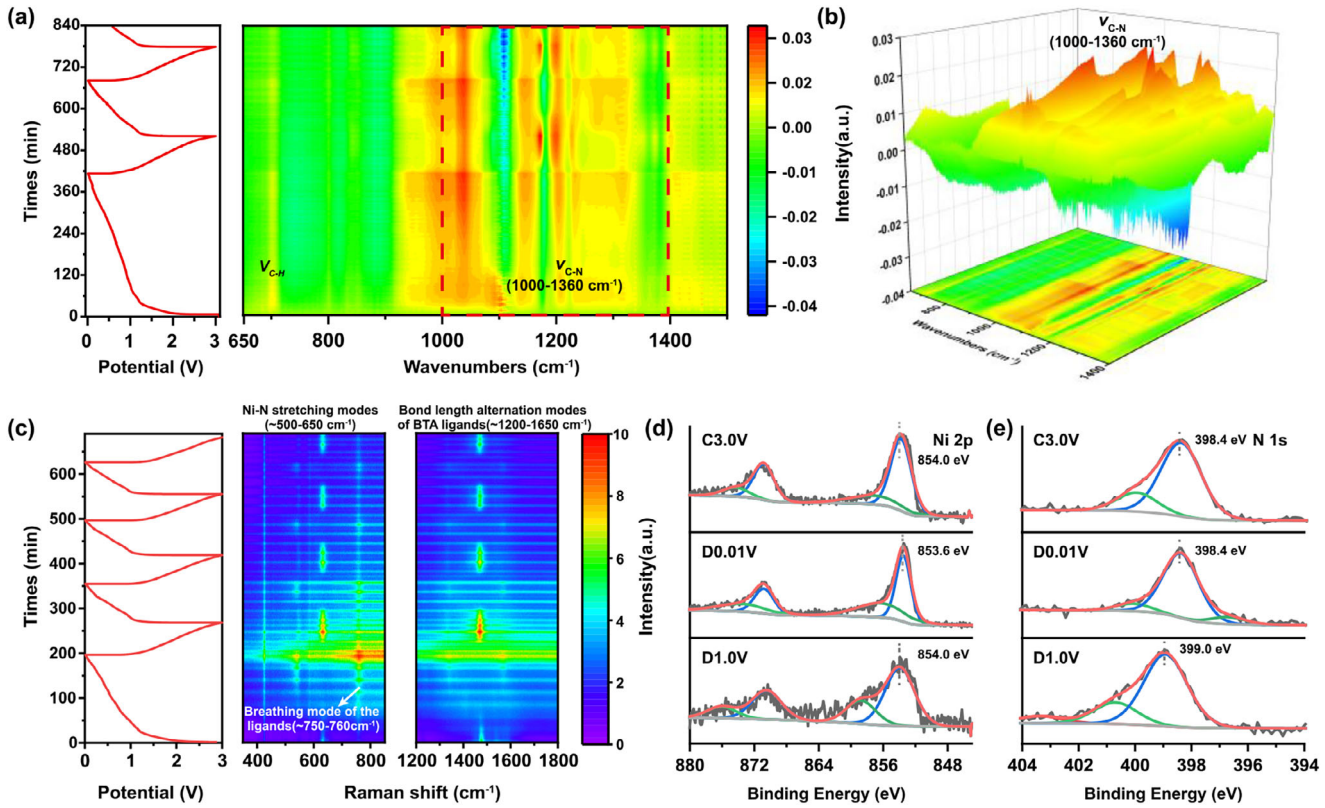

Figure 4. Identification of the potassium storage mechanism in the Ni-BTA during cycling. a) 2D map of in situ infrared structural evolution; b) 3D map; c) In situ Raman structural evolution; d,e) Ex situ XPS characterization of Ni-BTA: (d) High-resolution Ni 2p spectrum; (e) High-resolution N 1s spectrum.

In parallel with the investigation of bulk ion diffusion, Electrochemical Impedance Spectroscopy (EIS) was employed to probe the charge transfer kinetics at the electrode/electrolyte interface. Nyquist plots were collected at various states of charge and discharge after initial cycling (Figure S30a–f, Supporting information). In these plots, the diameter of the semicircle in the high-frequency region corresponds to the charge transfer resistance (Rct). A consistent trend is observed across all tested potentials: the Ni-BTA electrode consistently exhibits the smallest semicircle diameter, signifying the lowest Rct among the three materials. This distinction is particularly pronounced at deeper states of discharge (e.g., at 0.3 V), where the Rct of Ni-BTA is substantially smaller than that of its Co and Mn analogues. This reduced interfacial resistance indicates a more facile electron transfer process, which can be directly attributed to the higher intrinsic electronic conductivity of the Ni-BTA framework, a consequence of its enhanced π–d conjugation and narrower band gap.

In conclusion, these comprehensive kinetic studies reveal a dual advantage for the Ni-BTA anode. The superior rate capability and high capacity utilization are underpinned by a synergy of faster bulk K^+ diffusion, as evidenced by GITT, and more efficient interfacial charge transfer, as confirmed by EIS. Both of these favorable kinetic factors are fundamentally rooted in the unique electronic structure modulated by the Ni^{2+} center, providing a robust and comprehensive explanation for the material's exceptional overall electrochemical performance.

2.4. Potassium Storage Mechanism

The electrochemical potassium storage mechanism of Ni-BTA was systematically investigated through complementary spectroscopic and structural analyses. While previous studies demonstrated two-electron storage within 0.5–2.0 V,[51] the measured capacity of ≈460 mAh g^{-1} significantly exceeds the theoretical two-electron limit (278 mAh g^{-1}) even after subtracting carbon additive contributions (≈48 mAh g^{-1}, Figure S27, Supporting information), strongly suggesting a three-electron transfer process. Based on the molar mass of the $Ni[C_6H_2(NH)_4]$ repeating unit, a three-electron redox process would correspond to a theoretical capacity of 417 mAh g^{-1}, a value in excellent agreement with our experimental findings. This hypothesis was verified through in situ spectroscopic monitoring of structural evolution during cycling.

In situ FTIR and Raman spectroscopic analyses provide direct evidence of the ligand-dominated potassium storage mechanism in Ni-BTA. During discharge, progressive enhancement of C=N vibrations at 1381 cm^{-1} and aromatic ring oscillations at 1140 cm^{-1} was observed (**Figure** 4a,b), corresponding to K^+ adsorption on the Ni-N4 coordination sites. Complete signal recovery during charging confirmed reversible ion insertion/extraction. The intensified C=N vibration indicates that the σ-π hybridization between Ni's dx^2-y^2 orbitals and BTA ligand facilitates localized charge redistribution, thereby enhancing the ligand's ability to accommodate K^+. These findings were corroborated by

in situ Raman analysis showing characteristic Ni-N stretching (500–600 cm^{-1}), ligand breathing (750–760 cm^{-1}), and chain vibration (1200-1650 cm^{-1}) modes intensifying during potassium insertion and diminishing upon extraction (Figure 4c).[51] The reversible Ni-N bond vibration further validates that the $t_2g \rightarrow \pi$ back-donation stabilizes the coordination framework against structural distortion during cycling. The periodic nature of these spectral changes over the first four cycles, coupled with first-cycle capacity loss attributed to SEI formation rather than structural degradation, demonstrates exceptional framework reversibility.

The structural evolution during cycling was further investigated through a combination of ex situ XRD and DFT simulations. The ex situ XRD patterns collected at characteristic discharge voltages (1.3, 0.7, 0.3, and 0.01 V) reveal a progressive attenuation and broadening of the Bragg peaks, indicating a significant loss of long-range crystalline order, or partial amorphization, of the Ni-BTA framework upon deep potassiation (Figure S31, Supporting information). This experimental observation is powerfully explained by our DFT calculations (Figure S32, Supporting information), which show that the sequential incorporation of three K^+ ions induces a dramatic structural rearrangement and a stepwise molar volume expansion, ultimately reaching a substantial ≈48% increase (from 304.6 to 451.38 $Å^3$). This massive volume change, which typically triggers mechanical degradation in conventional electrode materials, is accommodated by the unique flexible molecular architecture of Ni-BTA, where the non-covalently bonded framework withstands strain through dynamic conformational adjustments rather than bond fracture.

Notably, upon recharging, the diffraction features are substantially recovered, indicating a highly reversible process. Intriguingly, the intensity of the recovered peaks can even exceed that of the pristine state. This suggests the process is best described as a reversible structural reconstruction rather than a simple restoration. During the charge-discharge cycles, the framework undergoes a form of "electrochemical annealing" and reorganization, potentially leading to a new, highly ordered texture with a preferred orientation of the polymer chains. This reorganization is a testament to the material's exceptional structural compliance and is considered a key factor in its outstanding long-term cycling stability.

Ex situ XPS analysis further corroborated the ligand-dominated potassium storage mechanism. Throughout various charge/discharge states, the Ni valence remained largely unchanged, exhibiting only a minor 0.4 eV reduction in binding energy, confirming negligible Ni participation in redox reactions (Figure 4d). This slight shift likely arises from charge density redistribution induced by K^+ adsorption, with filled t_2g orbitals suppressing metal-centered redox activity to ensure structural stability. Similarly, high-resolution N 1s spectra revealed a binding energy decrease from 399 eV to 398.4 eV upon discharge, attributed to SEI formation, with reversible modifications in C═N and C—N bonding configurations confirmed K^+ storage on the organic ligand (Figure 4e). Complementary ex situ EPR measurements provided additional evidence for electron uptake by the BTA ligand during K^+ insertion. The EPR signal intensity progressively diminished at discharged states (1.0, 0.01 V) but recovered upon charging (1.5, 3.0 V), whereas the g-value remained constant (2.002, Figure S33, Supporting information). Collectively, these observations suggest electron transfer to the ligand, reducing radical species and converting C═N bonds to C—N single bonds. Notably, the near-identical EPR intensities between fully charged and discharged states indicate highly reversible electron transfer, further demonstrating the structural and electronic stability of Ni-BTA during cycling.

The interfacial chemistry evolution was elucidated through time-of-flight secondary ion mass spectrometry (TOF-SIMS) with sub-100 nm depth resolution. In negative-ion mode, characteristic fragments corresponding to KF^- (m/z = 58.0), KF_2^- (78.0), $NOFS^-$ (145.1), NO_2S^- (146.0), and SO_3^- (163.1) were consistently identified at both fully discharged (D0.01 V) and fully charged (C3.0 V) states, matching the decomposition products of KFSI ($K[N(SO_2F)_2]$) electrolyte (Figure S34, Supporting information). Quantitative analysis demonstrated significantly higher signal intensities for KF^-, KF_2^-, $NOFS^-$, and NO_2S^- during discharge compared to charging, indicating that K^+ intercalation enhances surface accumulation of electrolyte decomposition products. This conclusion was further corroborated by 2D compositional mapping (Figure S35 and S36, Supporting information). This dense inorganic structure effectively inhibits further electrolyte decomposition.

In positive-ion spectra, distinct signals including $NOSF^+$ and K_2O^+ were detected with pronounced intensity in the near-surface region (**Figure 5**). The rapid attenuation of these signals with increasing sputtering depth indicates that fluorine-containing inorganic salts and oxide-like species are primarily localized in the outer SEI layers (Figure 5a,b). 2D mapping confirmed their uniform distribution, supporting the conclusion that the SEI consists predominantly of inorganic salts, consistent with the proposed role of KFSI in SEI formation (Figure 5d,e). Comparative analysis of TOF-SIMS data between discharged and charged states revealed enhanced signals of SEI-related ions (e.g., $NOSF^+$, K_2O^+) in the initial layers during discharge (Figure S37, Supporting information), suggesting more extensive electrolyte decomposition at low potentials, which promotes rapid formation of an inorganic-rich SEI (Figure 5d). In contrast, slight signal attenuation was observed during charging, likely due to partial SEI reconstruction or dissolution, leading to minor redistribution of surface species (Figure 5b,d). Notably, the Ni^+ signal remained consistently weak in both states, indicating that Ni centers in Ni-BTA are not exposed at the surface and do not participate in significant electrochemical reactions (Figure 5c). The electrochemical inertness of coordinated Ni atoms ensures structural integrity of the material framework. Even during continuous SEI reconstruction, the Ni-BTA structure remains stable, contributing to the superior cycling performance of Ni-BTA electrode.

2.5. Theoretical Calculation Analysis

To elucidate the potassium storage mechanism of the Ni-BTA electrode, first-principle calculations were systematically conducted to investigate the electronic structure evolution and kinetic behavior during K^+ intercalation.[52] DOS calculations using the HSE06 hybrid functional revealed a semiconductor characteristic with an ≈1 eV band gap near the Fermi level (**Figure 6a**), which is significantly more favorable for electron transport compared to the insulating nature of conventional organic materials. Analysis of K adsorption at different molecular chain sites

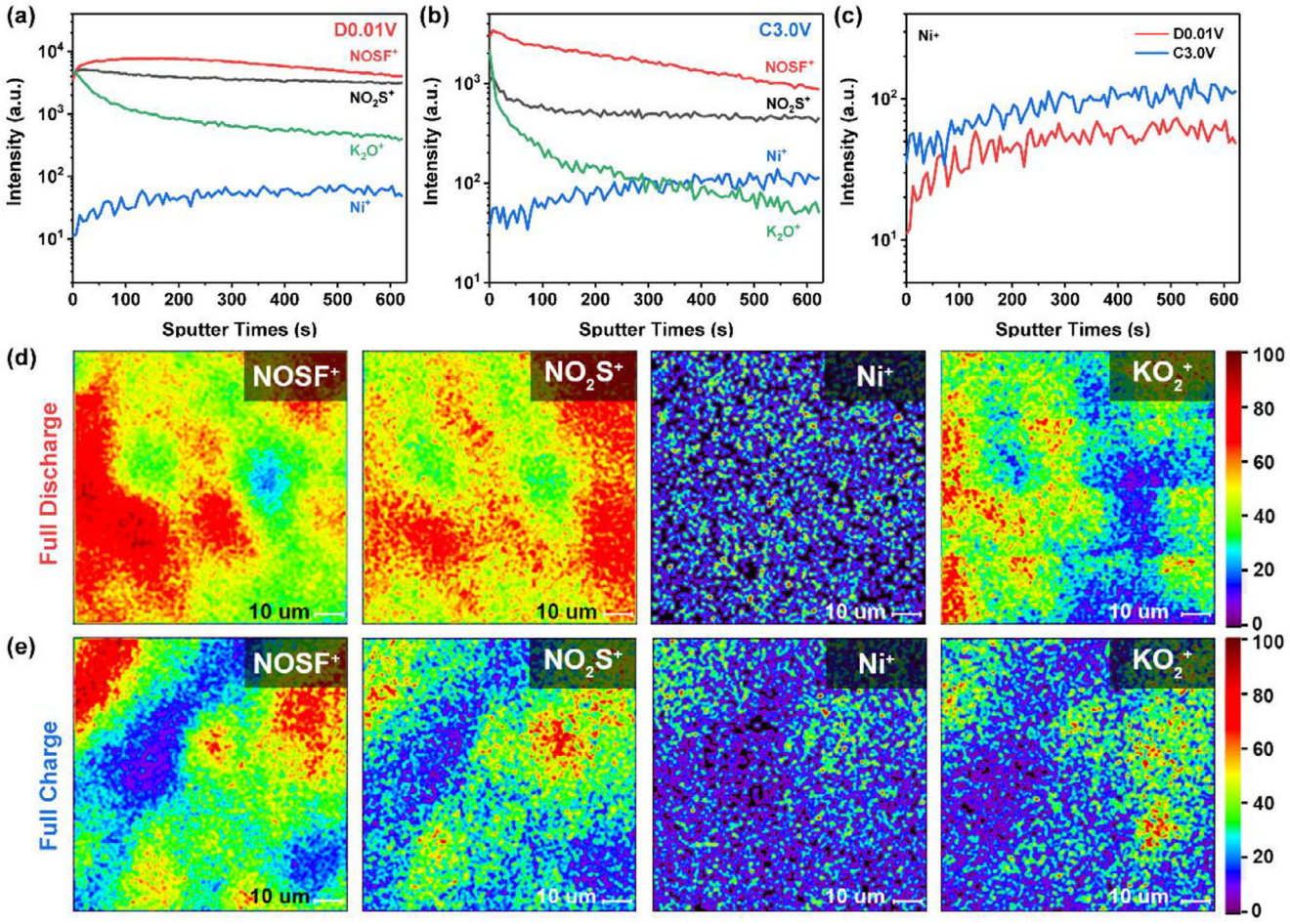

Figure 5. Positive-ion TOF-SIMS analysis of interfacial evolution in Ni-BTA electrode. a) Depth profiles of characteristic components ($NOSF^+/NO_2S^+/K_2O^+/Ni^+$) at 0.01V discharged state; b) Corresponding profiles at 3.0V charged state; c) Near-surface distribution of Ni^+ signals; d,e) 2D spatial mapping of $NOSF^+$ (left), NO_2S^+ (middle-left), Ni^+ (middle-right), K_2O^+ (right) components in fully (d) discharged and (e) charged states.

showed distinct spatial heterogeneity in adsorption energies. The strongest K adsorption was observed at S2 (−0.67 eV) and S3 (−0.67 eV) sites above nitrogen-containing five-membered rings, followed by the S4 site (−0.59 eV) between adjacent nitrogen atoms, while the S1 site (0.42 eV) above benzene rings exhibited positive adsorption energy, indicating K repulsion in this region (Figure 6b). Charge density difference analysis confirmed that K atoms lose electrons to form K^+ during adsorption, with electron acceptors primarily localized in nitrogen-rich heterocyclic regions (S2/S3 sites) of the BTA ligand, highlighting the synergistic potassium storage advantage of Ni metal centers and BTA ligands (Figure 6c). The stepwise voltage evolution from initial KNi-BTA to fully saturated K_3NiBTA showed plateaus at 1.42, 0.70, and 0.49 V, indicating stable single-atom K^+ intercalation rather than metal cluster formation, consistent with the smooth voltage plateaus observed in charge/discharge curves (Figure 6d). Diffusion kinetics studies revealed a migration barrier of 0.35 eV for K^+ along both the molecular chain (Path 1) and between adjacent units (Path 2), with higher barriers in benzene ring regions aligning with adsorption energy trends, further confirming nitrogen-rich heterocycles as the dominant active sites (Figure 6e,f). These multiscale computational results systematically elucidate the potassium storage characteristics and mechanism of Ni-BTA framework materials from electronic structure, thermodynamic stability, and kinetic perspectives.

To further clarify the redox nature of three-electron potassium storage, Hirshfeld charge analysis was also performed to examine charge redistribution at different intercalation stages (**Figure 7**). In the initial state, Ni atoms exhibited a significant positive charge (+1.09), balanced by four nitrogen atoms in the BTA ligand with −0.81 charge, forming a stable Ni–N_4 coordination structure and establishing a charge gradient for subsequent K^+ intercalation. During the first electron insertion, the charge of Ni center only slightly adjusted from +1.09 to +1.06, while adjacent nitrogen atoms experienced a sharp charge increase from −0.81 to −0.99, indicating that initial K^+ adsorption primarily involves charge exchange with ligand nitrogen sites. Notably, as the second and third K^+ ions were inserted, the Ni center's charge remained stable (±0.05 variation), confirming its structural support and charge buffering role. In contrast, ligand nitrogen charges exhibited dynamic evolution: increasing to −0.91 during the second electron insertion and readjusting to −0.96 upon the third, suggesting multielectron transfer primarily occurs within the BTA ligand. Notably, the total charge variation of nitrogen atoms (Δq

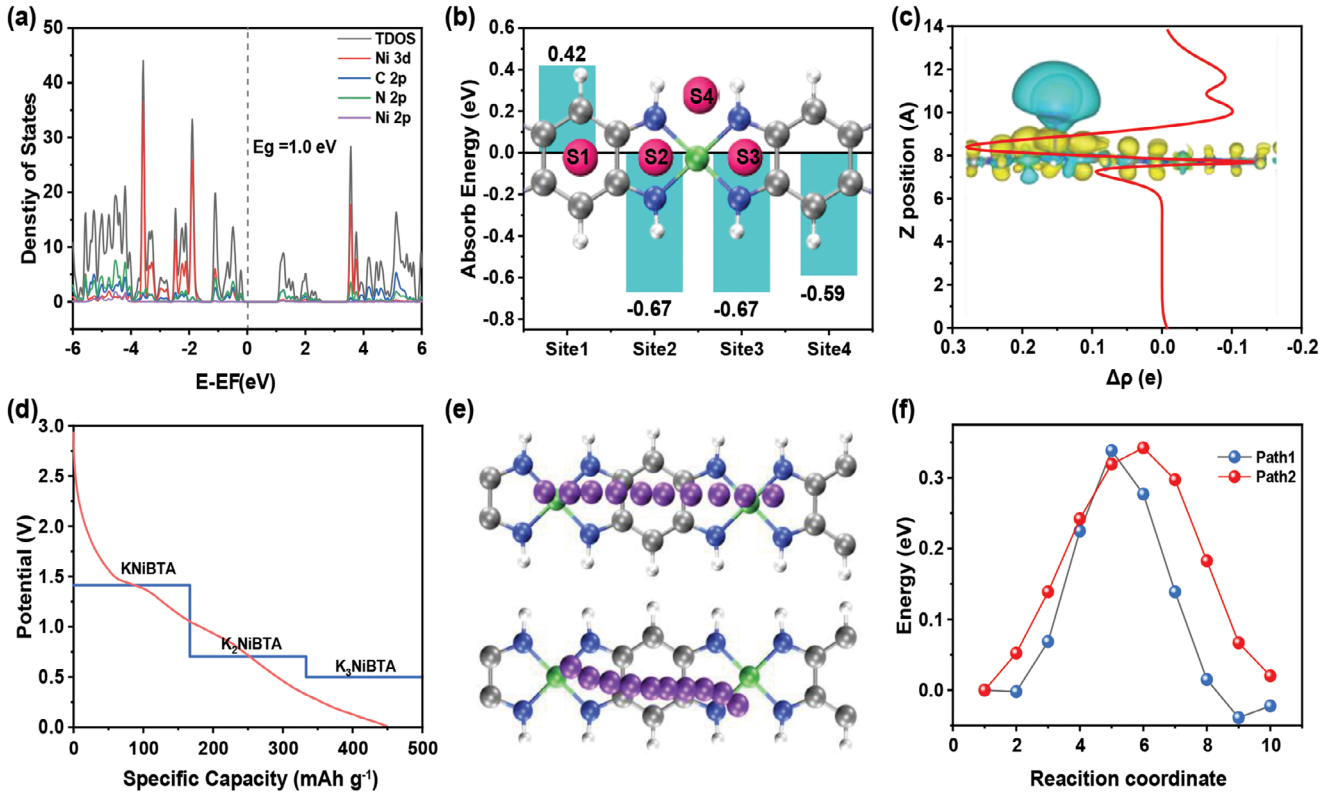

Figure 6. Theoretical calculations of the density of states and potassium adsorption characteristics for Ni-BTA. a) Density of states and projected density of states for Ni-BTA, b) Comparison of potassium adsorption energies at different sites on Ni-BTA, c) Potassium adsorption charge density difference maps of Ni-BTA, d) Comparison between the average potassium intercalation voltage and actual working voltage with the average lithium intercalation voltage, e) Schematic diagram of potassium diffusion pathways along the 1D Ni-BTA molecular chain, f) Migration energy barriers along different diffusion pathways on the Ni-BTA 1D molecular chain.

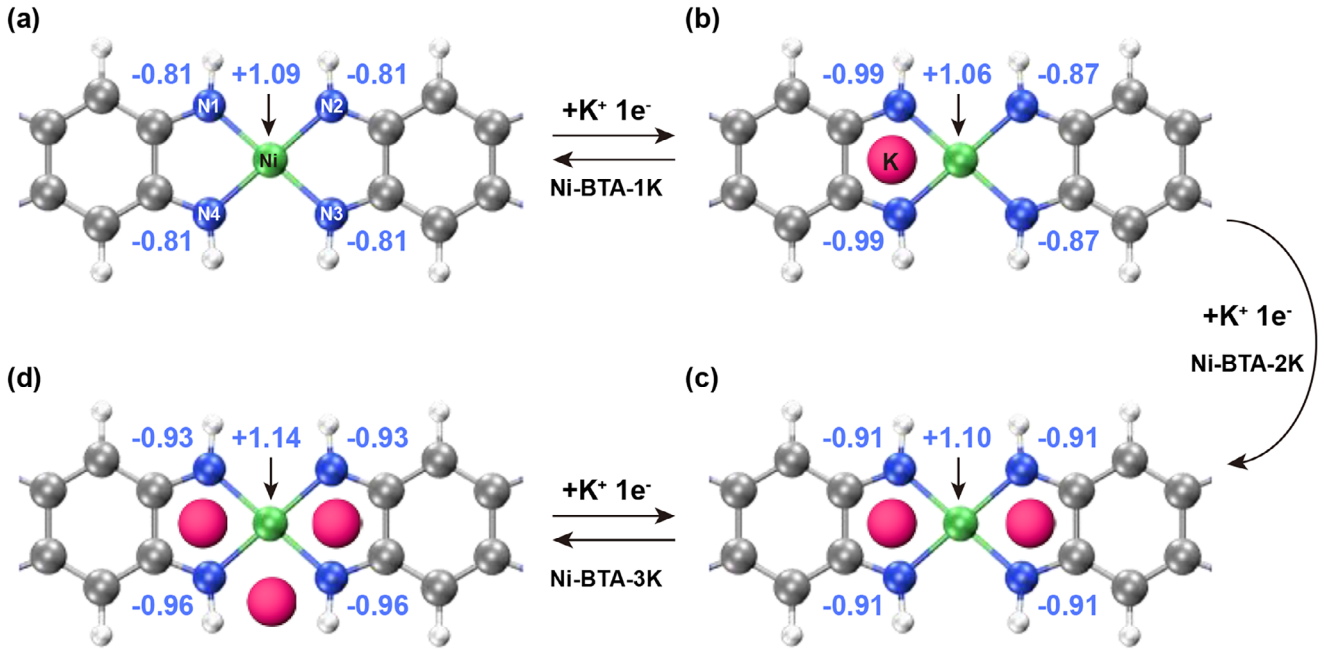

Figure 7. Schematics of the potassium storage mechanism in the Ni-BTA electrode and corresponding Hirshfeld charge evolution. a) Pristine state, b) first K^+ intercalation, c) second K^+ intercalation, d) third K^+ intercalation.

= 0.15 e^-) was three times greater than that of the Ni center (Δq = 0.05 e^-), directly demonstrating that redox activity originates mainly from ligand electron transfer rather than the metal center. The ligand-dominated three-electron redox behavior is fundamentally rooted in the dual electronic regulation intrinsic to Ni-BTA. The $t_2g \rightarrow \pi$ back-donation stabilizes the BTA framework by delocalizing electron density across the conjugated backbone during K^+ insertion, while σ-π hybridization between Ni $d_{x^2-y^2}$ orbitals and ligand π-systems facilitates efficient charge transfer. Such synergistic orbital interactions decouple redox activity from structural degradation: ligand-centered C═N/C—N transitions drive energy storage, whereas the closed-shell d^8 Ni^{2+} centers act as inert anchors to mitigate volume expansion. This strategic combination of d-orbital engineering and π-conjugation explains Ni-BTA's exceptional cycling stability and establishes a generalized design principle based on optimized transition metal d-orbital configurations, where t_{2g} occupancy governs electron delocalization and σ-π hybridizability dictates charge transfer kinetics. The principle is demonstrated to transcend conventional capacity-stability tradeoffs in π–d conjugated coordination polymers, with extensibility confirmed for multivalent ion storage systems requiring concurrent high energy density and durability.

3. Conclusion

In this work, we systematically demonstrate that d-orbital configuration engineering in π–d conjugated coordination polymers effectively addresses the long-standing trade-off between redox activity and structural stability in KIBs anodes. By selecting Ni^{2+} with a closed-shell d^8 configuration over paramagnetic Co^{2+} and Mn^{2+} counterparts, we achieve synergistic orbital interactions that simultaneously enhance charge transfer and framework stability. The $t_2g \rightarrow \pi$ back-donation mechanism stabilizes antibonding orbitals while σ-π hybridization between $d_{x^2-y^2}$ orbitals and BTA ligands reduces K^+ adsorption energy by 44% compared to Co/Mn analogues, as confirmed through combined experimental and theoretical analyses. These electronic effects translate to exceptional electrochemical performance, with Ni-BTA delivering a high reversible capacity of 452 mAh g^{-1} at 100 mA g^{-1} (99.2% retention over 500 cycles) and sustaining 292 mAh g^{-1} after 4000 cycles at 1000 mA g^{-1}. Notably, multimodal in situ characterization reveals that the nitrogen heterocycles in BTA ligands drive a three-electron redox process through reversible C═N/C—N transitions, while the electrochemically inert Ni centers act as structural pillars during cycling. This decoupling of redox-active and stabilizing roles fundamentally addresses the capacity-fading dilemma in conventional systems. Beyond advancing KIB technology, this work provides critical insights into orbital-level engineering for energy materials.

Supporting Information

Supporting Information is available from the Wiley Online Library or from the author.

Acknowledgements

This work was supported by the National Key Research and Development Program of China (2023YFB3809300), National Energy-Saving and Low-Carbon Materials Production and Application Demonstration Platform Program (TC220H06N), National Natural Science Foundation of China (52373306, 52472244 and 52127816), Natural Science Foundation of Hubei Province (2023AFA053).

Conflict of Interest

The authors declare no conflict of interest

Data Availability Statement

The data that support the findings of this study are available from the corresponding author upon reasonable request.

Keywords

π–d conjugation, conductive coordination polymers, ligand-dominated storage, potassium-ion batteries

Received: May 13, 2025
Revised: July 5, 2025
Published online:

[1] X. Yi, H. Fu, A. M. Rao, Y. Zhang, J. Zhou, C. Wang, B. Lu, *Nat. Sustain.* **2024**, *7*, 326.
[2] G. Ji, J. Wang, Z. Liang, K. Jia, J. Ma, Z. Zhuang, G. Zhou, H.-M. Cheng, *Nat. Commun.* **2023**, *14*, 584.
[3] S. Lv, X. Ma, S. Ke, Y. Wang, T. Ma, S. Yuan, Z. Jin, J.-L. Zuo, *J. Am. Chem. Soc.* **2024**, *146*, 9385.
[4] P. Cai, K. Wang, T. Wang, H. Li, M. Zhou, W. Wang, K. Jiang, *Adv. Energy Mater.* **2024**, *14*, 2401183.
[5] L. Fan, H. Xie, Y. Hu, Z. Caixiang, A. M. M. Rao, J. Zhou, B. Lu, *Energy Environ. Sci.* **2023**, *16*, 305.
[6] J. Lee, H. Lim, J. Park, M. Kim, J. Jung, J. Kim, I. Kim, *Adv. Energy Mater.* **2023**, *13*, 2300442.
[7] X. Ma, H. Fu, J. Shen, D. Zhang, J. Zhou, C. Tong, A. M. Rao, J. Zhou, L. Fan, B. Lu, *Angew. Chem., Int. Ed.* **2023**, *62*, 202312973.
[8] Q. Zhang, Z. Wang, S. Zhang, T. Zhou, J. Mao, *Z. Guo, Electrochem. Energy Rev.* **2018**, *1*, 625.
[9] G.-Z. Yang, Y.-F. Chen, B.-Q. Feng, C.-X. Ye, X.-B. Ye, H. Jin, E. Zhou, X. Zeng, Z.-L. Zheng, X.-L. Chen, D.-S. Bin, A.-M. Cao, *Energy Environ. Sci.* **2023**, *16*, 1540.
[10] Y. Xu, Y. Du, H. Chen, J. Chen, T. Ding, D. Sun, D. H. Kim, Z. Lin, X. Zhou, *Chem. Soc. Rev.* **2024**, *53*, 7202.
[11] H. Park, Y. Lee, W. Ko, M. Choi, B. Ku, H. Ahn, J. Kim, J. Kang, J. Yoo, J. Kim, *Batter. Supercaps* **2023**, *6*, 202200486.
[12] L. Fan, Q. Liu, S. Chen, K. Lin, Z. Xu, B. Lu, *Small* **2017**, *13*, 1701011.
[13] D. Liu, Z. Yang, W. Li, S. Qiu, Y. Luo, *Electrochim. Acta* **2010**, *55*, 1013.
[14] W. Zhang, J. Ming, W. Zhao, X. Dong, M. N. Hedhili, P. M. F. J. Costa, H. N. Alshareef, *Adv. Funct. Mater.* **2019**, *29*, 1903641.
[15] J. Hu, Y. Hong, M. Guo, Y. Hu, W. Tang, S. Xu, S. Jia, B. Wei, S. Liu, C. Fan, Q. Zhang, *Energy Storage Mater.* **2023**, *56*, 267.
[16] J. Bitenc, K. Pirnat, O. Lužanin, R. Dominko, *Chem. Mater.* **2024**, *36*, 1025.
[17] S. Gu, J. Chen, I. Hussain, Z. Wang, X. Chen, M. Ahmad, S. Feng, Z. Lu, K. Zhang, *Adv. Mater.* **2024**, *36*, 2306491.
[18] A. U. Mu, G. Cai, Z. Chen, *Adv. Sci.* **2024**, *11*, 2305280.
[19] X. Tang, C. Liu, H. Wang, W. Sun, Y. Wang, *Coord. Chem. Rev.* **2023**, *494*, 215361.

[20] H. Xu, P. Geng, W. Feng, M. Du, D. J. Kang, H. Pang, *Nano Res.* **2024**, *17*, 3472.
[21] J. Zhou, R. C. K. Reddy, A. Zhong, Y. Li, Q. Huang, X. Lin, J. Qian, C. Yang, I. Manke, R. Chen, *Adv. Mater.* **2024**, *36*, 2312471.
[22] B. Sun, Z. Sun, Y. Yang, X. L. Huang, S. C. Jun, C. Zhao, J. Xue, S. Liu, H. K. Liu, S. X. Dou, *ACS Nano* **2023**, *18*, 28.
[23] X. Yang, L. Gong, K. Wang, S. Ma, W. Liu, B. Li, N. Li, H. Pan, X. Chen, H. Wang, J. Liu, J. Jiang, *Adv. Mater.* **2022**, *34*, 2207245.
[24] E. R. Wolfson, L. Schkeryantz, E. M. Moscarello, J. P. Fernandez, J. Paszek, Y. Wu, C. M. Hadad, P. L. McGrier, *ACS Appl. Mater. Interfaces* **2021**, *13*, 41628.
[25] S. Wang, Q. Wang, P. Shao, Y. Han, X. Gao, L. Ma, S. Yuan, X. Ma, J. Zhou, X. Feng, B. Wang, *J. Am. Chem. Soc.* **2017**, *139*, 4258.
[26] Z. Liu, T. Liu, C. N. Savory, J. P. Jurado, J. S. Reparaz, J. Li, L. Pan, C. F. J. Faul, I. P. Parkin, G. Sankar, S. Matsuishi, M. Campoy-Quiles, D. O. Scanlon, M. A. Zwijnenburg, O. Fenwick, B. C. Schroeder, *Adv. Funct. Mater.* **2020**, *30*, 2003106.
[27] Y. Chen, M. Tang, Y. Wu, X. Su, X. Li, S. Xu, S. Zhuo, J. Ma, D. Yuan, C. Wang, W. Hu, *Angew. Chem., Int. Ed.* **2019**, *131*, 14873.
[28] Y. Chen, Q. Zhu, K. Fan, Y. Gu, M. Sun, Z. Li, C. Zhang, Y. Wu, Q. Wang, S. Xu, J. Ma, C. Wang, W. Hu, *Angew. Chem., Int. Ed.* **2021**, *60*, 18769.
[29] K. Fan, C. Zhang, Y. Chen, Y. Wu, C. Wang, *Chem* **2021**, *7*, 1224.
[30] L. Lin, Y. Ni, L. Shang, H. Sun, Q. Zhang, W. Zhang, Z. Yan, Q. Zhao, J. Chen, *ACS Catal.* **2022**, *12*, 7531.
[31] Y. Ni, L. Lin, Y. Shang, L. Luo, L. Wang, Y. Lu, Y. Li, Z. Yan, K. Zhang, F. Cheng, J. Chen, *Angew. Chem., Int. Ed.* **2021**, *60*, 16937.
[32] Y. Wan, Y. Sun, X. Wu, J. Yang, *J. Phys. Chem. C* **2018**, *122*, 989.
[33] S. Takaishi, M. Hosoda, T. Kajiwara, H. Miyasaka, M. Yamashita, Y. Nakanishi, Y. Kitagawa, K. Yamaguchi, A. Kobayashi, H. Kitagawa, *Inorg. Chem.* **2009**, *48*, 9048.
[34] K. Fan, J. Li, Y. Xu, C. Fu, Y. Chen, C. Zhang, G. Zhang, J. Ma, T. Zhai, C. Wang, *J. Am. Chem. Soc.* **2023**, *145*, 12682.
[35] L. Wang, Y. Ni, X. Hou, L. Chen, F. Li, J. Chen, *Angew. Chem., Int. Ed.* **2020**, *59*, 22126.
[36] Z. Pan, X. Huang, Y. Fan, S. Wang, Y. Liu, X. Cong, T. Zhang, S. Qi, Y. Xing, Y.-Q. Zheng, J. Li, X. Zhang, W. Xu, L. Sun, J. Wang, J.-H. Dou, *Nat. Commun.* **2024**, *15*, 9342.
[37] Y. Lian, W. Yang, C. Zhang, H. Sun, Z. Deng, W. Xu, L. Song, Z. Ouyang, Z. Wang, J. Guo, Y. Peng, *Angew. Chem. Int. Ed.* **2020**, *59*, 286.
[38] C. Wang, H. Dong, L. Jiang, W. Hu, *Chem. Soc. Rev.* **2018**, *47*, 422.
[39] A. Savin, R. Nesper, S. Wengert, T. F. Fässler, *Angew. Chem., Int. Ed.* **1997**, *36*, 1808.
[40] T. Lu, Q. Chen, *Chemistry–Methods* **2021**, *1*, 231.
[41] Z. Sang, J. Liu, X. Zhang, L. Yin, F. Hou, J. Liang, *ACS Nano* **2023**, *17*, 3077.
[42] S. Shang, C. Du, Y. Liu, M. Liu, X. Wang, W. Gao, Y. Zou, J. Dong, Y. Liu, J. Chen, *Nat. Commun.* **2023**, *14*, 190.
[43] A. P. Grosvenor, M. C. Biesinger, R. St C Smart, N. S. McIntyre, *Surf. Sci.* **2006**, *600*, 1771.
[44] M. Cheng, H. Fan, Y. Song, Y. Cui, R. Wang, *Dalton Trans.* **2017**, *46*, 9201.
[45] Z. Huang, J. Liu, Y. Liu, Y. Xu, R. Li, H. Hong, L. Shen, H. Lin, B.-Q. Liao, *J. Membr. Sci.* **2021**, *623*, 119080.
[46] Y. Gao, Y. Yang, R. Schimmenti, E. Murray, H. Peng, Y. Wang, C. Ge, W. Jiang, G. Wang, F. J. DiSalvo, D. A. Muller, M. Mavrikakis, L. Xiao, H. D. Abruña, L. Zhuang, *Proc. Natl. Acad. Sci.* **2022**, *119*, 2119883119.
[47] P. Talebi, A. A. Kistanov, E. Rani, H. Singh, V. Pankratov, V. Pankratova, G. King, M. Huttula, W. Cao, *Appl. Energy* **2022**, *322*, 119461.
[48] A. Wang, S. Kadam, H. Li, S. Shi, Y. Qi, *Npj Comput. Mater.* **2018**, *4*, 15.
[49] S. Li, Y. Liu, L. Dai, S. Li, B. Wang, J. Xie, P. Li, *Energy Storage Mater.* **2022**, *48*, 439.
[50] X.-L. Chen, M. Xie, Z.-L. Zheng, X. Luo, H. Jin, Y.-F. Chen, G.-Z. Yang, D.-S. Bin, D. Li, *J. Am. Chem. Soc.* **2023**, *145*, 5105.
[51] R. R. Kapaev, A. Zhugayevych, S. V. Ryazantsev, D. A. Aksyonov, D. Novichkov, P. I. Matveev, K. J. Stevenson, *Chem. Sci.* **2022**, *13*, 8161.
[52] R. Pawar, A. A. Sangolkar, *Comput. Theor. Chem.* **2021**, *1205*, 113445.
[53] S. Sarkar, J. S. Won, M. An, R. Zhang, J. H. Lee, S. G. Lee, Y. L. Joo, *Polymers* **2022**, *14*, 1342.
[54] N. Solati, M. Çankaya, A. Kahraman, K. Şimşek, C. J. Titus, S. J. Lee, D. Nordlund, H. Ogasawara, A. Tekin, S. Kaya, *Materials Today Energy* **2023**, *35*, 101323.
[55] Z. Xiao, J. Meng, F. Xia, J. Wu, F. Liu, X. Zhang, L. Xu, X. Lin, L. Mai, *Energy Environ. Sci.* **2020**, *13*, 3129.